Journal of Materials Chemistry A

Ab initio determination of a simultaneous dual-ion charging mechanism for $Ni_{0.25}Mn_{0.75}O_2$ through redox reactions of Ni^{2+}/Ni^{4+} and O^{2-}/O^{-}

Journal:	*Journal of Materials Chemistry A*
Manuscript ID	TA-ART-05-2022-003938.R1
Article Type:	Paper
Date Submitted by the Author:	20-Jul-2022
Complete List of Authors:	Shepard, Robert; Alvernia University, Mathematics and Technology; Binghamton University, Physics Brennan, Scott; Binghamton University, Physics Juran, Taylor; Binghamton University, Physics Young, Joshua; New Jersey Institute of Technology, Department of Chemical and Materials Engineering Smeu, Manuel ; Binghamton University, Physics

Journal Name

ARTICLE TYPE

Cite this: DOI: 00.0000/xxxxxxxxxx

Ab initio determination of a simultaneous dual-ion charging mechanism for $Ni_{0.25}Mn_{0.75}O_2$ through redox reactions of Ni^{2+}/Ni^{4+} and O^{2-}/O^{-}†

Robert Shepard,[a,b] Scott Brennan,[a] Taylor Juran,[a] Joshua Young,[a,c] and Manuel Smeu[a,*]

Received Date
Accepted Date

DOI: 00.0000/xxxxxxxxxx

Over recent years, great efforts have been made to push the limits of layered transition metal oxides for secondary battery cathodes. This is particularly true for overall capacity, which has reached a terminal theoretical value for many materials. One avenue for increasing this capacity during charging is the intercalation of anions post cation deintercalation. This work investigates the charging mechanism of the P3-$Na_{0.5}Ni_{0.25}Mn_{0.75}O_2$ cathode material through cation (Na) deintercalation and anion (ClO_4) intercalation by means of density functional theory. The calculations corroborate experimental findings of increased capacity (135 mAh g^{-1} to 180 mAh g^{-1}) through the intercalation of anions. However, this work demonstrates that a process of simultaneous cation deintercalation/anion intercalation is the primary charging mechanism, with charge compensation reactions of Ni^{2+}/Ni^{4+} and O^{2-}/O^{-} occurring within the cathode material. To elucidate this simultaneous process, a novel method for computationally determining anion voltage in which one must consider full electrolyte interactions is proposed. Based on the results, it is believed that a simultaneous cation deintercalation/anion intercalation mechanism provides one potential avenue for the discovery of the next generation of secondary batteries.

1 Introduction

The Li ion battery (LIB)[1–7] has long been held as the industry standard for powering portable electronics[8]. While it is believed that LIBs will never completely be replaced, many studies into alternative secondary batteries have been undertaken[8–16]. To start, investigation into Na would be prudent; the monovalent nature of both ions, abundance of Na, and similar chemical/electronic properties between Li and Na would make it a great choice[17,18]. Although Na mimics Li in many aspects, advancement of Na ion batteries (NIBs) is not without adversity.

Many materials have shown the ability to act as a cathode for NIBs, such as various oxides (*i.e.*, layered, olivine, and spinel), phosphates, and chalcogenides[15,16,19–23]. These materials have been shown to possess the ability to reach 4.5 V and obtain 300 mAh g^{-1} in various studies[24 and references therein]. However, such performance is rare; on average, NIBs fail to outperform the industry standard of 3.7 V and 372 mAh g^{-1} of LIBs. That is, of course, unless we go beyond the performance achieved with full extraction/intercalation of sodium. This raises the question on how one could continue further if all ions have been extracted. The answer lies with anions; the process of deintercalating cations is electronically equivalent to intercalating anions.

Recently, an experimental study by Li *et al.*[25] investigated the layered transition metal oxide (TMO) P3-$Na_{0.5}Ni_{0.25}Mn_{0.75}O_2$ for use as a Na ion battery (NIB) cathode. They found that after extracting all Na ions, ClO_4 would intercalate, thereby increasing capacity beyond what is theoretically predicted for Na ion participation alone. Specifically, they obtained a final capacity of 180 mAh g^{-1} (a ∼34% increase over the all-Na theoretical capacity of 134 mAh g^{-1}), which corresponds to an overall voltage of 4.15 V when charging their system. Furthermore, Li *et al.* proposed a multi-step process for cycling $Ni_{0.25}Mn_{0.75}O_2$ during which Ni species undergo a reversible cationic redox reaction ($Ni^{2+} \leftrightarrow Ni^{4+}$) and O atoms undergo a reversible anionic redox reaction ($O^{2-} \leftrightarrow O^{-}$).

To the best of the authors' knowledge, only two other computational studies have investigated ClO_4 intercalation. However, these works investigated intercalation into graphite, with the focus of their calculations solely on the physical and electronic structure changes during intercalation; no electrochemical performance was determined through density functional theory

---

[a] *Department of Physics, Binghamton University - SUNY, 4400 Vestal Parkway East, Binghamton, NY 13902, United States.*

[b] *Department of Mathematics and Technology, Alvernia University, 400 Saint Bernardine Street, Reading, PA 19607, United States.*

[c] *Department of Chemical and Materials Engineering, New Jersey Institute of Technology, 323 Dr. Martin Luther King Jr. Boulevard, Newark, NJ 07102, United States.*

* Corresponding author: msmeu@binghamton.edu

† Electronic Supplementary Information (ESI) available: [details of any supplementary information available should be included here]. See DOI: 00.0000/00000000.

(DFT)[26,27]. Additionally, several studies can be found with ClO_4 present in various electrolytes, again focusing on physical and electronic properties and not electrochemical performance[28–31]. The work presented here will involve both intercalation within the $Ni_{0.25}Mn_{0.75}O_2$ cathode and the ion-electrolyte interactions present within a realistic system.

2 Compuational Methods

2.1 Computational details

In this work we investigate the processes of Na deintercalation and ClO_4 intercalation within the layered TMO of P3-$Ni_{0.25}Mn_{0.75}O_2$ (referred to simply as NMO hereafter) when paired with a Na metal anode and propylene carbonate (PC) electrolyte, by means of computational modeling based in DFT[32–38]. To accomplish this, physical structures, density of states (DOS), cell voltages, diffusion barriers, and charge analyses are all calculated with various forms of the exchange-correlation (xc) functional and van der Waals (vdW) correction schemes. Specifically, the generalized gradient approximation (GGA) by Perdew, Burke, and Ernzerhof (PBE)[39] and the strongly constrained and appropriately normed (SCAN)[40] functionals, and the DFT-D3[41] and rVV10[42,43] vdW corrections were used. In addition, the rotationally invariant approach to the Hubbard U correction, as introduced by Dudarev *et al.*[44,45], was employed in conjunction with the PBE-D3 xc functional-vdW correction combination to accurately account for the on-site Coulomb interactions of transition metal (TM) 3(d) electrons. This combination was utilized only in electronic structure calculations revolving around the investigation of computationally demonstrating the charge compensation redox reactions of NMO (see Sec. 3.4), with values of U=4.0 eV for Mn and 6.0 eV for Ni. The decision to utilize the Hubbard U correction only for the investigations of redox reactions was based on previous computational investigations[46–50] which demonstrated its effectiveness in describing TMOs.

DFT calculations were performed using the Vienna *Ab initio* Simulation Package (VASP)[51], which utilizes a plane wave basis set in the expansion of the Kohn-Sham single particle wave functions. The ion-electron interactions were approximated using the projector augmented wave (PAW) potentials[52] with non-spherical contributions from gradient corrections inside the PAW spheres included. Both the kinetic energy cutoff and Γ-centered Monkhorst-Pack[53] k-point grid were tested independently for convergence against a 1-meV/atom threshold. It was determined that a 700-eV kinetic energy cutoff and a $3 \times 3 \times 1$ k-point grid were sufficient for the NMO unit cell (shown in Fig. 1). Appropriate smearing methods were used for sampling the Brillouin zone for intercalated and empty NMO structures, including the Methfessel-Paxton[54] method. For electronic structure investigations (*i.e.*, DOS), the previous methods and the tetrahedron method with Blöchl corrections[55] were utilized. All structural relaxations and energy calculations were performed using the conjugate-gradient algorithm[56] with the inclusion of electron spin (*i.e.*, spin polarization). The ground state configuration was considered reached upon net forces on atoms falling below 0.01 eV/Å. Each system was modeled and analyzed using the Visualization for Electronic and STructural Analysis (VESTA) software[57].

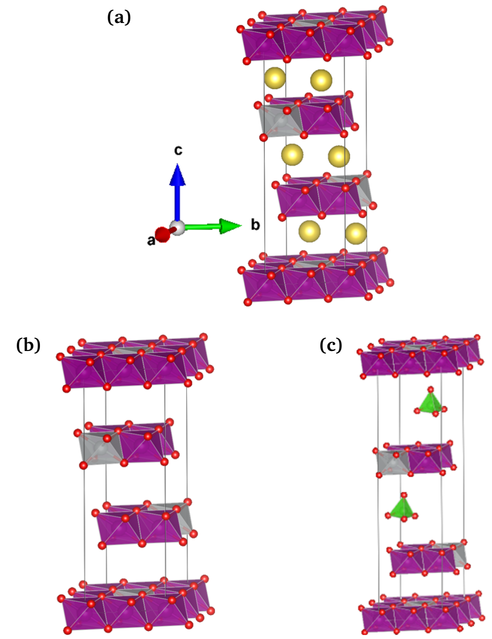

Fig. 1 The $R\bar{3}m$ unit cells of (a) $Na_{0.5}Ni_{0.25}Mn_{0.75}O_2$, (b) $Ni_{0.25}Mn_{0.75}O_2$, and (c) $Ni_{0.25}Mn_{0.75}O_2(ClO_4)_{0.167}$ used in this work. As the discharged cathode (*i.e.*, $Na_{0.5}Ni_{0.25}Mn_{0.75}O_2$) was synthesized in the P3 phase[25], such a structure was used for the empty and ClO_4-intercalated systems. Nickel atoms are shown in gray, manganese in purple, and oxygen in red. NOTE: The three panels are not to scale.

2.2 Relaxations

Full structural relaxations (including lattice vectors) were completed on empty and cation/anion-intercalated NMO structures (see Fig. 1) using the PBE, PBE-D3, PBE-D3+U, SCAN and SCAN-rVV10 xc-vdW approximations, as mentioned in Sec. 2.1. Concentrations between $x = 0.083$ and $x = 0.5$, inclusive, were used for simulating intercalation of Na in Na_xNMO. These concentrations correspond to 1 and 6 ions, respectively, in our simulation cells. Additionally, $x = 0.5$ is referred to as the "fully sodiated" concentration hereafter.

For the intercalation of ClO_4, concentrations of $y = 0.083$ and $y = 0.167$ (*i.e.*, 1 and 2 molecules, repsectively) in NMO$(ClO_4)_y$ were investigated. Intercalation of ClO_4 was halted at $y = 0.167$ (referred to as "fully perchlorated" hereafter) based on the previously reported percentage increase in overall capacity as compared to that obtained from full desodiation[25]. Ion intercalation was completed via a series of independent site testing, the details of which are discussed in Sec. S1 & S2†.

2.3 Nudged Elastic Band

Ion migration in NMO was investigated for both Na and ClO_4, individually, using the nudged elastic band (NEB) method[58–65] with PBE-D3. The migration pathways investigated (shown in Fig. 3a & 3b) were based on the results of the site testing discussed in Sec. S1 & S2†. To simulate ion migration, a $2 \times 2 \times 1$ supercell was created to allow each NEB pathway to start and end at an equivalent site (*i.e.*, the lowest energy position of a single Na or ClO_4) and to create sufficient distance (*i.e.*, ∼10 Å) between repeated images to greatly reduce any interactions between them. Unique pathways were individually tested and combined in such a way to show ion migration throughout the NMO interlayer space. The use of this method allowed migration of both Na and ClO_4 along similar, although not identical, pathways. A total of 7 images were used to sample along each migration pathway.

2.4 *Ab initio* Molecular Dynamics

To determine the energies of our electrolyte systems, we performed *ab initio* molecular dynamics (AIMD)[66–69] simulations. To simulate the electrolyte, AIMD calculations were completed on a simulation cell consisting of 24 PC molecules and 0, 1, 2, or 3 $NaClO_4$ units (shown in Fig. S3†), all of which were randomly distributed throughout the simulation cell. For each system containing $NaClO_4$ salt, the proximity of Na to ClO_4 was investigated (including both contact and solvent-separated ion pairs) and each system was designed to correspond to densities previously reported for $NaClO_4$ in PC based on molarity (both explicitly determined by, and interpolated from, experiment)[70,71]. Molarity and density data for these systems are provided in Table S1†.

The AIMD simulations were run at 350 K with 1-fs time steps using the canonical (NVT) ensemble[72–77]. First, each system was equilibrated for 5 ps; following this, an additional 2 ps of simulation time was performed. Frozen images were taken from each 2-ps simulation in increments of 0.1 ps and the total energy of each was computed self-consistently. The final total energy was then taken through two methods; 1) as the average of these 20 image energies and 2) an average of the entire 2-ps AIMD trajectory. For all AIMD calculations, only the Γ k-point was used and vdW interactions were included via the Grimme D3 approach[41] (*i.e.*, PBE-D3).

2.5 Voltage

Once all relaxation and AIMD energies are obtained, voltage can then be calculated. In previous computational works, it has been demonstrated that the average voltage for a secondary battery can be calculated as

$$V = \frac{-\Delta G}{nF}, \tag{1}$$

where ΔG is the difference in Gibbs free energy between the charged and discharged states, n is the number of electrons transferred during intercalation, and F is Faraday's constant[78–84]. Although ΔG can explicitly be calculated, we approximate it as equal to the internal energy (*i.e.*, DFT determined ground state energy) for this work. This approximation is expected not only to save on the overall computational costs for this investigation, but to be accurate (*i.e.*, within 0.2 V of the "true" voltage[78,82,84]) as well.

The approximation above allows Eqn. 1 to be rewritten in the general form of,

$$V = \frac{E_{\text{charged}} - E_{\text{discharged}}}{\#\text{ of } e^- \text{ transferred}}, \tag{2}$$

where E_{charged} is the sum of energies of the components in the charged state and $E_{\text{discharged}}$ is the sum of energies of the components in the discharged state. When intercalating cations, Eqn. 2 becomes,

$$V = \frac{(E_y + (x-y)E_{\text{metal}}) - E_x}{(x-y)Z}, \tag{3}$$

where E_y and E_x are the energies of NMO intercalated with y and x cations (where $x > y$), respectively, E_{metal} is the energy per atom of the pure cation-metal anode, and Z is the valency of the intercalated cation ($Z = 1$ for Na). To ensure conformity to thermodynamic principles, Eqn. 3 is only applied to those cation intercalation concentrations residing on a convex hull of formation energies[15,16]. When intercalating anions, however, Eqn. 3 is no longer applicable due to the intercalated ion (ClO_4 in this work) not having a solid metal counterpart. Here, we revisit Eqn. 2 and expand based on a novel approach developed in part from previous computational work which also investigated anion voltage[85–90].

In the present work, we begin our anion voltage calculations by considering the Na metal anode, ClO_4-intercalated cathode, and electrolyte with lower molarity of salt as components of the charged state (see Fig. 2c). The components of the discharged state (with respect to ClO_4) are then an electrolyte with a higher molarity of salt and the empty NMO structure (see Fig. 2b). This is represented mathematically by Eqn. 4 and shown schematically in Fig. 2.

In Eqn. 4, the first, second, and fifth terms are all found as described in Sec. 2.2, where E_{Na} is the energy per atom of the pure Na metal anode, $E_{\text{NMO},(x-y)\text{ClO}_4}$ is the energy of NMO intercalated with $(x-y)$ (where $x > y$) ClO_4 molecules, and E_{NMO} is the energy of the empty NMO structure. The third and fourth terms in Eqn. 4 represent the PC electrolyte with y and x salt pairs, respectively. This equation was utilized to simulate charging from the empty NMO structure to the fully perchlorated one, as originally proposed by Li *et al.*[25]. However, as discussed in Sec. 3.3, Eqn. 4 will require modification to accommodate a novel charging mechanism proposed by this work.

To the best of the authors' knowledge, only four other groups have reported on the computation of anionic voltages. However, many of these other works did not model a true representation of the electrolyte with salt; they employed a molecular species model[85–89]. One group did simulate such a realistic electrolyte model of salt in solvent, but their work did not involve a change in molarity of salt but a change in anionic species from $AlCl_4^-$ to $Al_2Cl_7^-$[90].

$$V = \frac{((x-y)E_{\text{Na}} + E_{\text{NMO},(x-y)\text{ClO}_4} + E_{24\text{PC},y\text{NaClO}_4}) - (E_{24\text{PC},x\text{NaClO}_4} + E_{\text{NMO}})}{(x-y)e^-} \tag{4}$$

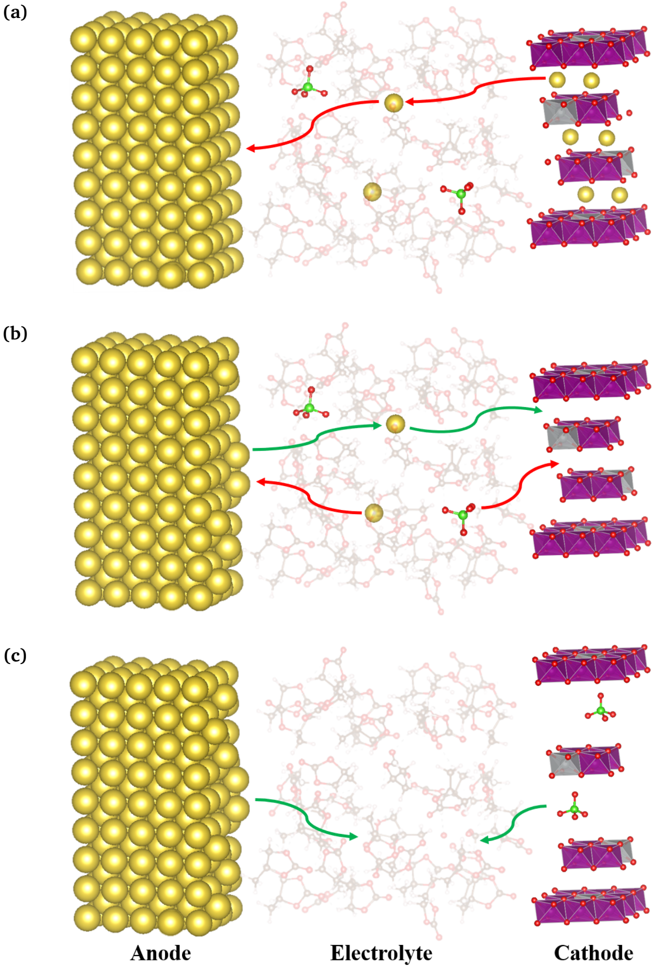

Fig. 2 Structural models of the anode, electrolyte, and cathode for different stages of the initially investigated charging mechanism of full desodiation followed by perchlorate intercalation. This charging "path" (*i.e.*, (a)→(b)→(c)) is denoted with red arrows, while the discharge mechanism ((c)→(b)→(a)) is shown with green arrows.

2.6 Charge Compensation Reactions

During the charging cycle of NMO, charge compensation reactions involving cationic ($Ni^{2+} \leftrightarrow Ni^{4+}$) and anionic ($O^{2-} \leftrightarrow O^{-}$) redox reactions have been shown to occur[25]. Therefore, the ability to computationally capture and accurately model these reactions is of particular interest in this work. To investigate these proposed reactions, DOS, oxidation state determination through the use of the density derived electrostatic and chemical (DDEC6) charges approach[91–99] in conjunction with ligand field theory[100], Bader charge analysis, and structural deformations (*i.e.*, changes in X– O bond lengths, where X = Mn, Ni, O) are all computed to determine the computational validity of these charge compensation mechanisms.

3 Results

3.1 Structural Characterization

As stated in Sec. 2.2, full structural relaxations were completed for the fully sodiated NMO structure using an assortment of xc functionals, both with and without additonal vdW correction terms. The numerical results of these calculations can be found in Table S2†, with a full comparison between them and experiment[25] in Sec. S4†. In short, we conclude that the xc functional of PBE (without the inclusion of vdW corrections) yields best overall agreement. Discussion on the structural characterization for the fully perchlorated structure can also be found in Sec. S4†, with additional anion intercalation investigations discussed in Sec. S5†.

3.2 Ion Migration Barriers

Diffusion barriers were calculated for both Na and ClO_4, individually, as outlined in Sec. 2.3. A combination of four individually calculated pathways (shown in Fig. 3a & 3b for Na and ClO_4, respectively) are combined to represent ion migration throughout the NMO interlayer space. The combination of these plots is shown in Fig. 3c, where it is evident that both Na and ClO_4 are freely able to diffuse (with barriers < 0.1 eV) through the interlayer spacing of NMO; corroborating the experimental claim that both ions readily intercalate within the bulk[25].

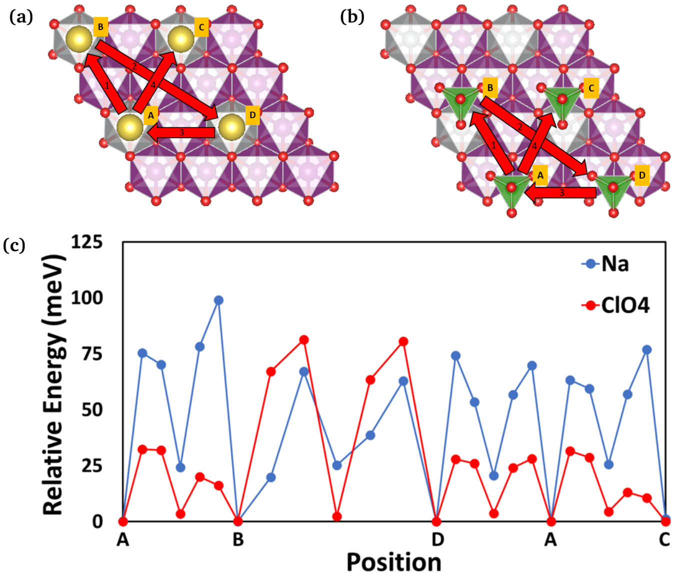

Fig. 3 The four individual migration pathways investigated for (a) Na and (b) ClO_4. The energetics of these pathways were combined following the pathway of A→B→D→A→C (*i.e.*, numerical order of red arrows in (a) and (b)) to create the diffusion barrier plot in (c). For both Na and ClO_4, diffusion barriers calculated with PBE-D3 are well below the theoretically determined threshold of 0.525 eV from Rong *et al.*[101].

3.3 Electrochemical Performance

Due to the structural match between our calculations for Na intercalation and experiment (and how closely the empty and ClO_4-intercalated structures match that of Na-intercalated for the a and b lattice vectors), only PBE-D3 was used in all voltage calculations in this work. The decision to include D3 was based on the desire to more accurately account for interactions occurring within the electrolyte simulation cells, in turn more accurately determining the voltage profile.

We began our electrochemical investigation with the process

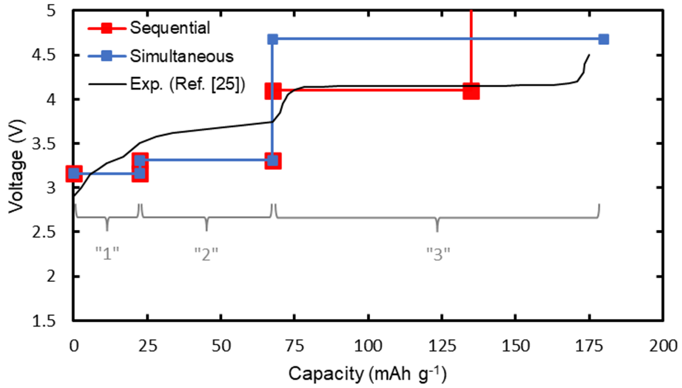

Fig. 4 Voltage profiles for charging NMO from $Na_{0.5}Ni_{0.25}Mn_{0.75}O_2$ to $Ni_{0.25}Mn_{0.75}O_2(ClO_4)_{0.167}$ for this work are shown as red and blue lines, which are discussed in Sec. 3.3. The reported voltage profile of Li *et al.*[25] has been adapted and included as a black line. Also labeled are the three distinct charging plateaus.

of full desodiation followed by perchlorate intercalation, as was the suggested mechanism reported by Li *et al.*[25]. Their reported voltage profile (which was adapted and included in Fig. 4 as a black line) consists of three distinct plateaus during charging. These plateaus approximately run from 0–22, 22–67, and 67–180 mAh g^{-1}, respectively, and are labeled on Fig. 4. In their analyses (*e.g.*, Field-Emission Transmission Electron Microscopy and X-ray Diffraction), Li *et al.* demonstrated the NMO cathode contained only Na cations when discharged and only ClO_4 anions when charged. These two end points of charging correspond to our fully sodiated and fully perchlorated structures (shown in Fig. 1a & 1c, respectively). It is the middle region (*i.e.*, partially charged) that is the focus of this investigation as it was not comprehensively characterized previously.

For the desodiation process, formation energies were determined and a corresponding convex hull (Fig. S7†) was constructed. Next, a voltage profile (red data points in Fig. 4) was created utilizing Eqn. 3 for those points residing on the convex hull. Complete desodiation corresponds to the voltage profile from 0 to 134 mAh g^{-1}. From the empty NMO structure, ClO_4 intercalation was then simulated. The voltages were calculated for a variety of simulated systems, as discussed in Sec. 2.4 & 2.5. All voltages obtained for charging from empty NMO to ClO_4-intercalated are shown in Table S4†. All of those voltages are well above the experimentally reported[25] value of ∼4.15 V for the third charging plateau, with some values as high as 6 V. The resulting voltage profile for the combination of sequential desodiation and subsequent perchloration is shown as the red line Fig. 4.

From Fig. 4, we noticed how the first two plateaus are of appropriate width (*i.e.*, capacity range), despite the fact they are an underestimation of the experimental voltage. Due to the discrepancy between calculated and experimental voltage, one needs to consider the validity of Eqn. 3. However, we are confident in this method as it has provided excellent agreement to experiment in previous works[11,12,15,16,102,103]. The third plateau, however, is broken when following the process of full desodiation and then perchloration such that the voltage corresponding to perchlorate intercalation into empty NMO is well above the experimentally reported value. Therefore, we propose an alternative mechanism to that of Li *et al.*[25] in which the sequence of cation deintercalation/anion intercalation is investigated.

Our electrochemical investigation shifted to the possibility and plausibility of a charging mechanism that was not sequential in nature. That is, one in which cation deintercalation and anion intercalation was occurring simultaneously. As one potential mechanism, the first two plateaus are kept the same as the sequential mechanism (*i.e.*, 6→5→3 Na ions, for our supercell). At this partially charged state, half of the total Na has been removed. Then, in one simultaneous step, the remaining Na is to be removed while all of the ClO_4 is inserted. However, in order to calculate the voltage for this new mechanism, we need to revisit Eqn. 4.

Here, we propose a modification to the constituents included in the charged and discharged states. For a simultaneous mechanism, there may exist Na and ClO_4 within our cathode at the start and end of a given charging step. As such, Eqn. 4 requires modification to account for this possibility. We therefore present Eqn. 5 below. Here, all terms are defined as before. Now, y and j (x and i) are the number of Na and ClO_4 units, respectively, within the charged (discharged) cathode. Similarly, β (α) is the number of salt pairs within the charged (discharged) electrolyte. These two new variables are taken as $\{\alpha, \beta\} = \{3,2\}$ and $\{2,1\}$, with corresponding voltages calculated for both sets and averaged. This is done to simulate the voltage around the average of 2 salt pairs in our simulated electrolyte, which corresponds to a 1M concentration (as used by Li *et al.*[25] and shown in Table S1†). Additionally, $\gamma = (x-y)+(j-i)$, which equates to the number of electrons transferred within the charging reaction shown in Eqn. 6 below. If an investigated charging step involves a process such that $(j-i) = 2$ (*i.e.*, the largest value it can have for our simulation cell), then a single voltage is calculated for $\{\alpha, \beta\} = \{3,1\}$; this again keeps the 1M average for electrolyte molarity. If $(j-i) = 0$ (*i.e.*, only Na deintercalation occurs), then $\alpha = \beta$ and those terms are dropped from Eqn. 5. Utilizing our new equation, we are now able to compute the voltage of our initially proposed simultaneous mechanism of going from partially sodiated ($x = 3$ and $i = 0$) to fully perchlorated ($y = 0$ and $j = 2$). The result of this charging mechanism is shown in Fig. 4 as a blue line, which results in a voltage profile that qualitatively matches the experimental result much better, having a continuous (*i.e.*, unbroken) third plateau.

With this result, the proposed mechanism of simultaneous Na

$$V = \frac{\left(\gamma E_{\mathrm{Na}} + E_{\mathrm{NMO},y\mathrm{Na},j\mathrm{ClO_4}} + E_{\mathrm{24PC},\beta\mathrm{NaClO_4}}\right) - \left(E_{\mathrm{24PC},\alpha\mathrm{NaClO_4}} + E_{\mathrm{NMO},x\mathrm{Na},i\mathrm{ClO_4}}\right)}{\gamma e^{-}} \tag{5}$$

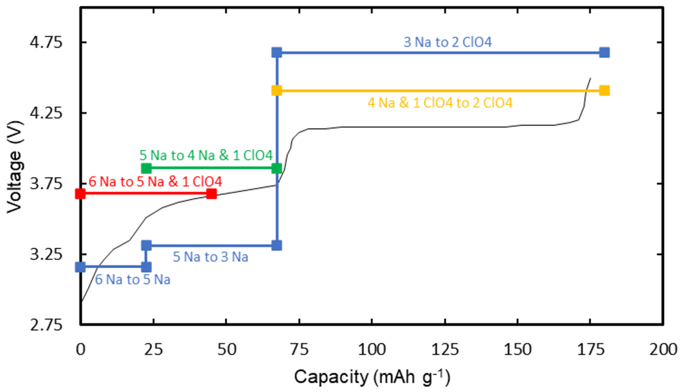

Fig. 5 A subset of some of the numerous potential steps to charge from $Na_{0.5}Ni_{0.25}Mn_{0.75}O_2$ to $Ni_{0.25}Mn_{0.75}O_2(ClO_4)_{0.167}$ investigated in this work. The reported voltage profile of Li *et al.*[25] has been adapted and included as a black line.

deintercalation and ClO_4 intercalation was now of great interest. A thorough search of the literature determined that the process of simultaneous cation deintercalation/anion intercalation within the same material is a novel idea with only one other work stating its possibility[104] (others have reported it for different electrodes[105]). Based on this novel idea, we began investigating various pathways from fully sodiated to fully perchlorated involving several simultaneous processes. A telling, non-exhaustive, summary of these results is provided in Fig. 5.

Inspection of Fig. 5 reveals several key insights into the proposed charging mechanism for NMO. For the first charging plateau (0–22 mAh g^{-1}), it can be seen that Na deintercalation alone (blue line) results in a voltage mostly below that of experiment (black line). However, when coupled with simultaneous intercalation of ClO_4 (*i.e.*, 1 molecule or half of the total amount of ClO_4 based on our simulation cell used), an increase in voltage is observed (red line). It is understood that this process does not correspond to the same capacity range for the first plateau; it is simply a consequence of the available combinations/concentrations of our simulated cells. Therefore, it is believed the actual process for this first charging step to be a mix of Na removed and ClO_4 inserted.

It is evident for the second plateau (22–67 mAh g^{-1}) of charging that desodiation alone (blue line) yields a voltage too low yet again and that a simultaneous process (green line) yields a voltage higher than experiment. For this step, it is our belief that one-sixth of the total Na is removed from the NMO material, while one-quarter of the total ClO_4 is inserted. It should be noted that these concentrations are based on those available within our supercell. However, we suspect the true concentrations be quite close to those proposed above.

Finally, the last (and largest) plateau of the charging process (67–180 mAh g^{-1}) demonstrates two things. First, the voltage obtained from intercalating 100% of the perchlorate (blue line) or the remaining 50% of the perchlorate (after 50% of the perchlorate is already interclated; yellow line) resulted in voltages that are too high (by 0.53 V and 0.26 V, respectively). Secondly, the voltage obtained when more Na is removed and less ClO_4 is inserted yields better agreement with experiment (*i.e.*, the yellow line compared to the blue line).

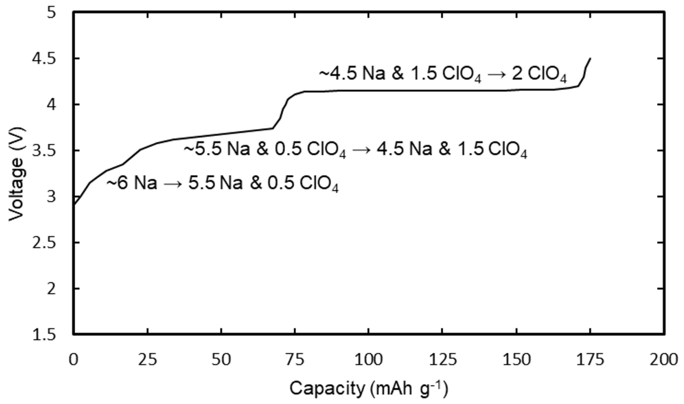

Fig. 6 The proposed mechanism for charging from $Na_{0.5}Ni_{0.25}Mn_{0.75}O_2$ to $Ni_{0.25}Mn_{0.75}O_2(ClO_4)_{0.167}$ through simultaneous cation (Na) deintercalation and anion (ClO_4) intercalation for the voltage profile of Li *et al.*[25] (adapted and included as a black line). NOTE: The number of each ion represented here is based on those concentrations available with the simulation cells utilized in this work.

Based on the previously discussed steps, we propose the actual charging mechanism for NMO from fully sodiated to fully perchlorated is that as shown in Fig. 6, in which we have adapted and included the reported voltage profile from Li *et al.*[25]. It would be ideal to compute the voltage for the proposed dual ion concentrations presented in Fig. 6. However, such concentrations require simulation cells beyond what could be handled with the available computational resources. It is to the best of our knowledge that this proposed mechanism is the first account of a computational claim of simultaneous cation deintercalation/anion intercalation within the same cathode material. With this newly proposed charging mechanism, and the previous claims of redox charge compensation reactions, we turn our investigation to determine how NMO electronically responds to each of these intercalated ions.

3.4 Charge Compensation Response of NMO

The following investigations and analyses are completed for the fully sodiated to empty to perchlorated charging mechanism, in apparent contradiction with our proposed mechanism in the previous section. However, the choice to investigate the following methods in this manner was deliberate to isolate the effects of cation deintercalation from those of anion intercalation, allowing us to determine which ion plays the major contributing role in the charge compensation reactions proposed. As discussed in Sec. 2.1, all charge compensation investigations utilize the PBE-

$$\mathrm{NMO}_{x\mathrm{Na},i\mathrm{ClO_4}} + \mathrm{PC}_{\alpha\mathrm{NaClO_4}} \rightarrow \mathrm{NMO}_{y\mathrm{Na},j\mathrm{ClO_4}} + \mathrm{PC}_{\beta\mathrm{NaClO_4}} + \gamma\mathrm{Na}\,. \qquad (6)$$

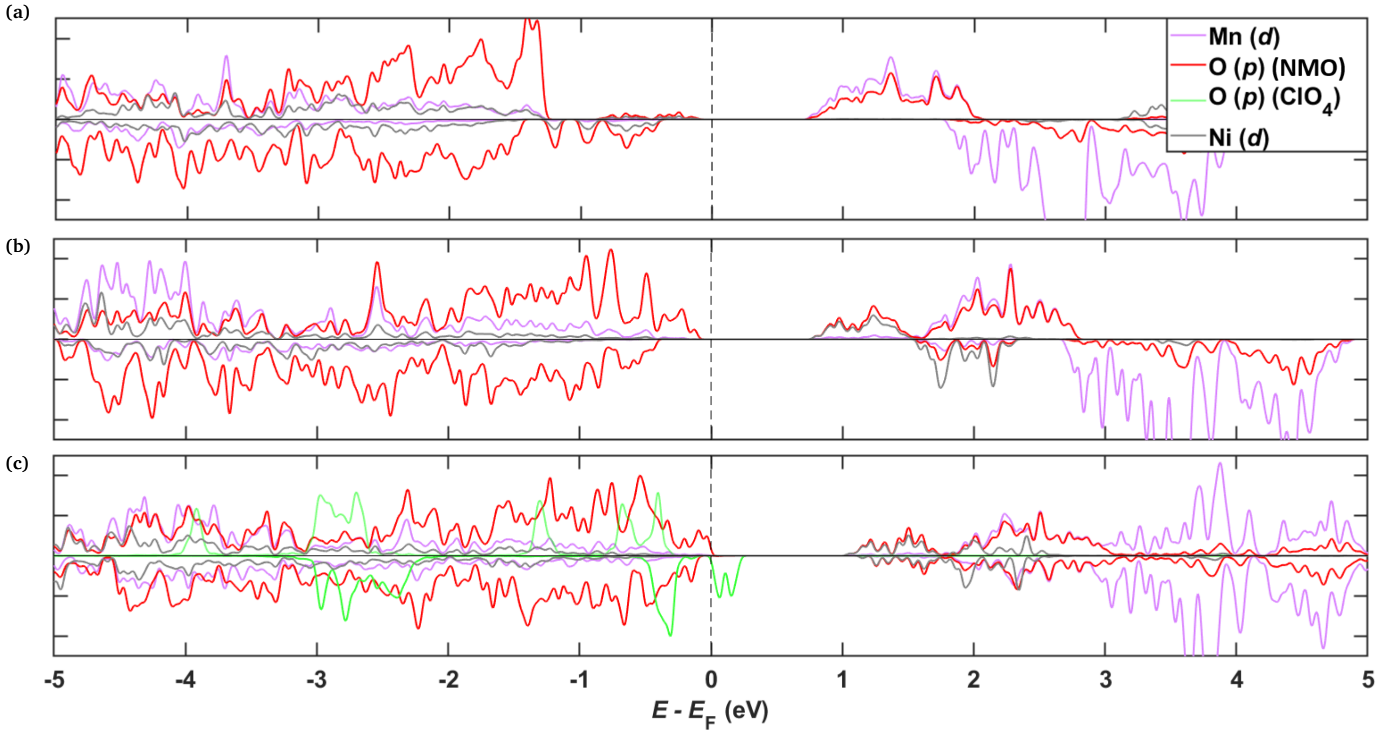

Fig. 7 Atom-resolved density of states (PDOS) for (a) $Na_{0.5}Ni_{0.25}Mn_{0.75}O_2$, (b) $Ni_{0.25}Mn_{0.75}O_2$, and (c) $Ni_{0.25}Mn_{0.75}O_2(ClO_4)_{0.167}$. Each of these plots was calculated using PBE-D3+U. NMO oxygens have been separately plotted from those of ClO_4 in plot (c). The Fermi level is indicated by the vertical dashed lines.

D3+U combination for their respective calculations.

3.4.1 Density of States

We begin with the electronic structure of the fully sodiated NMO system. As shown in Fig. 7a, there is a high level of hybridization between the TM(d) states and O(p) states. Such hybridization indicates a strong covalent character of the TM–O bonds[106]. Consequently, this indicates O redox is more likely to occur than TM redox[107]. When inspecting the states slightly below the Fermi level ($-1 \leq E - E_F \leq 0$), one can see that mainly O(p) and Ni(d) states contribute to these energies. As such, one would expect the Ni–O bonds to be the redox active centers during desodiation[46].

In the electronic structure of empty NMO (Fig. 7b), a drastic increase in contributions from O(p) states can be seen just below the Fermi level. This shift to higher energies is indicative of O atoms compensating for the charge removed during cation deintercalation, as previously reported[46,49,50,106–110]. Concurrent with this change, Ni(d) states have emptied and shifted to the conduction band (around 1 to 2 eV), indicating Ni atoms are compensating for charge removal during cation deintercalation[46,47,50,108,110,111].

Lastly, Fig. 7c presents the electronic structure of the fully perchlorated structure. From the claim of Li *et al.*[25], and others in literature[46,47,50,106–109], it was expected to see further redox activity of O(p) states. Comparing Fig. 7c to Fig. 7b, one can see that no significant change in any Ni, Mn, or lattice O atoms occurs. However, there is interesting behavior of the O atoms contained within ClO_4. For these states, we see high levels of hybridization with all other atoms throughout the displayed energy range, as well as significant contribution to those states near the Fermi level; behaviors indicative of some level of redox activity.

Throughout the charging process, the character of the Mn(d) states remains unchanged, indicating that Mn takes no part in any redox reactions present in our system. This is expected as further oxidation of Mn^{4+} to Mn^{5+} is highly unfavorable energetically for Mn atoms in octahedral coordination geometries. Although a small increase in Mn character can be seen just below the Fermi level during desodiation, we attribute this to lattice O coordinated with Mn undergoing redox. As the TM(d) and O(p) states are strongly hybridized, this change is Mn character is not unreasonable. As such, the PDOS of Mn throughout the charging process are deemed to be the typical charge order of Mn^{4+}.

From our electronic structure investigation for the fully sodiated, empty, and fully perchlorated systems, we conclude that Mn atoms within all systems maintains a Mn^{4+} oxidation state. For the desodiation portion of the charging process, clear changes in electronic character of Ni(d) and O(p) states suggests simultaneous $Ni^{2+} \rightarrow Ni^{4+}$ and $O^{2-} \rightarrow O^{-}$ transitions. Additionally, it would appear the O atoms on ClO_4 experience some nature of redox. However, further investigation into this intriguing observation is necessary prior to any definitive claims of such redox activity. To corroborate our other redox activity findings, we move to investigate the electronic nature of all atoms by their net magnetization through the use of the DDEC6 method.

3.4.2 DDEC6

To further examine the oxidation state of Ni, Mn, and O atoms in our fully sodiated, empty, and fully perchlorated NMO systems, we calculated the net spin moments on all atoms following the DDEC6 method[91–99]. However, the net spin moment is insufficient to determine oxidation state on its own. One must follow ligand field theory[100] (the more accurate modification of crystal field theory[112,113]) to take this spin moment and determine the oxidation state it corresponds to[49,50,106–108,111]. A description of this process is given in Sec. S7†, where electronic configurations for Ni and Mn are presented in Fig. S8 & S9†, respectively. From these electronic configurations, we expect to obtain a value of 3 μ_B for a Mn^{4+} oxidation state, and a value of 2/0 μ_B for a Ni^{2+}/Ni^{4+} oxidation state. However, it has been reported[111] that these numbers may be closer to 2.75 μ_B for a Mn^{4+} and 1.5 μ_B for Ni^{2+} due to the TM(d) and O(p) orbital hybridization discussed in Sec. 3.4.1.

The results of all net spin moment determinations are presented in Fig. 8. To start, we focus on Mn in the fully sodiated and empty NMO structures. Here, the Mn atoms average a net spin moment of 3.24 and 3.26 μ_B, respectively, matching a previously reported value[106]. Moving to the perchlorated system, we see a slight increase (3.4 μ_B). As with the PDOS of Sec. 3.4.1, this slight change could be attributed to the coordinated O atoms' redox activity and is unlikely an indication of a shift towards Mn^{5+} due to the energetic favorability of Mn^{4+} in the octahedral geometry.

For Ni atoms, there is a clear change from the Ni^{2+} oxidation state to that of Ni^{4+} during desodiation, with a further decrease in net spin moment during perchlorate intercalation. However, like those changes for Mn, these variations for Ni during perchlorate intercalation are minimal, most likely due to coordinated O redox activity, and the corresponding values match those previously reported[106].

Although ligand field theory is not applied, the net spin moments for O atoms were investigated for sake of completeness and are included on Fig. 8 as well. For both desodiation and perchlorate intercalation, there are negligible changes. The reason no change in net spin moment is found for O is likely due to the hybridization of the TM(d) and O(p) states and choice of functional combination. Any changes that do occur for O are overshadowed by the drastic changes occurring on the Ni atoms. Additionally, electrons from neighboring atoms could be captured with the inclusion of the D3 correction, effectively canceling out any spin moments on O (as well as leading to the overestimation for Mn and Ni atoms).

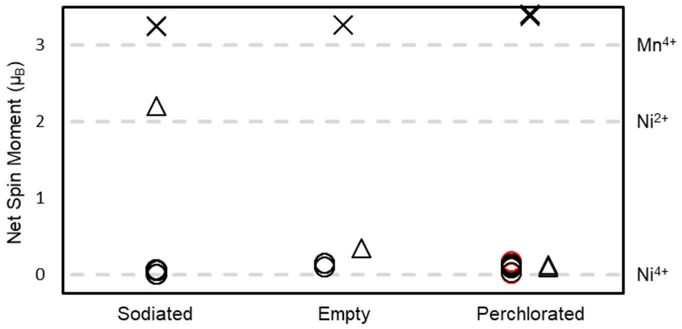

Fig. 8 Net spin moments for Ni (△), Mn (×), and O (○) atoms in fully sodiated, empty, and fully perchlorated NMO when calculated with PBE-D3+U. Shown on the right are the corresponding oxidation states for the Ni and Mn atoms. The red circles for the fully perchlorated system denote oxygen atoms within ClO_4.

Thus far, PDOS and net spin moments have been investigated to find evidence of charge compensation redox reactions. What these methods highlight is that no single method should be used in the determination of electronic structure. Various methods should be used in conjunction to fully understand the underlying electronic structure and any fluctuations therein. To this end, we move to further investigate/corroborate the suspected charge compensation reactions of $Ni^{2+} \rightarrow Ni^{4+}$ and $O^{2-} \rightarrow O^{-}$, as well as the inactivity of Mn, through Bader charge analysis.

3.4.3 Bader Charge Analysis

For Bader charge analysis, we are not specifically interested in the absolute value obtained from this method. Instead, we seek to find how the quantity changes during the charging process. It is this change that will indicate potential redox activity. The calculated Bader charge for all atoms within our three systems are presented in Fig. 9. To accentuate any changes that occur in the data, Fig. 9a & 9b zoom in on the Ni/Mn and O Bader charges, respectively. For both plots, two dashed lines represent linear fits for subsets of the data. One subset is the fully sodiated and empty systems, the other being those data for the empty and fully perchlorated systems.

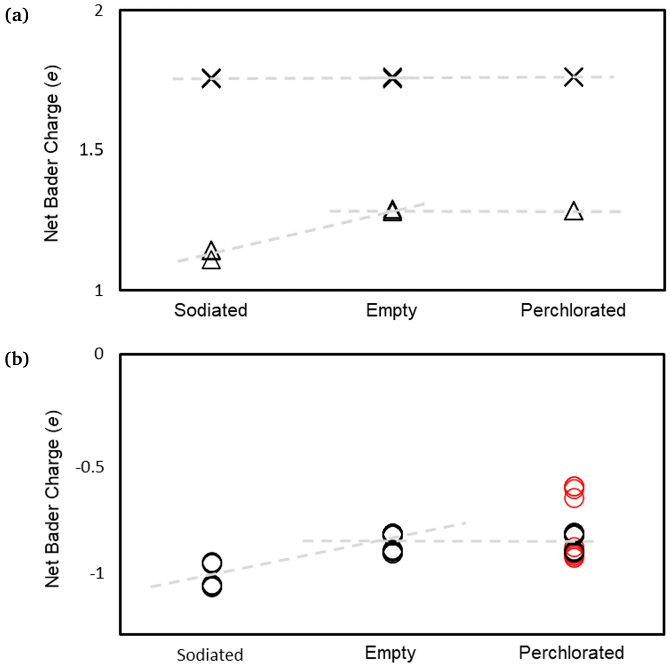

Fig. 9 Bader charge analysis for (a) Ni (△), Mn (×), and (b) O (○) atoms in fully sodiated, empty, and fully perchlorated NMO when calculated with PBE-D3+U. The red circles for the fully perchlorated system in (b) denote the oxygen atoms within ClO_4. Also shown are linear-fits (discussed in Sec. 3.4.3) to accentuate changes.

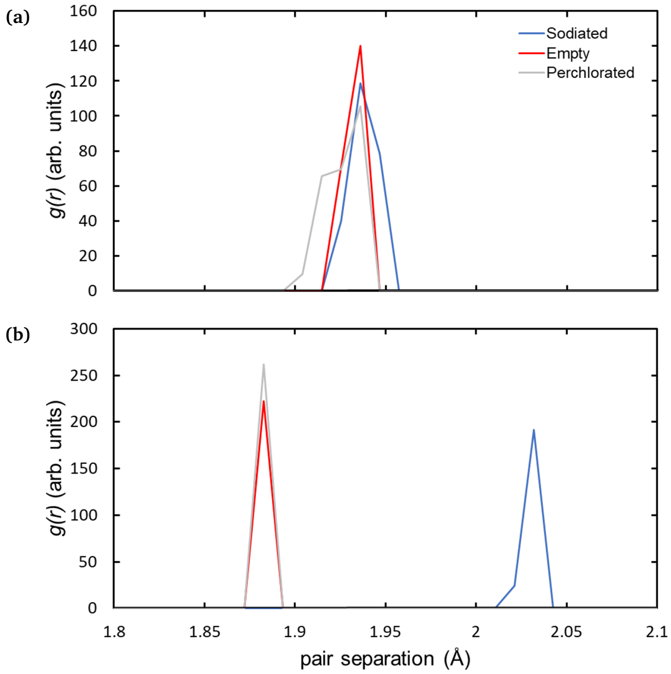

Fig. 10 Radial distribution, $g(r)$, plots of (a) Mn–O and (b) Ni–O bonds within the fully sodiated, empty, and fully perchlorated structures when relaxed with PBE-D3+U.

In Fig. 9a, Mn maintains a consistent value across all stages of charging. For Ni, however, a clear discontinuity occurs at the empty NMO system. For desodiation, a change of $\sim$0.16e occurs on Ni atoms, which matches changes others have previously reported for similar systems[49,106]. It should be noted that such a change (specifically, a change $< 0.2e$) has been reported as insignificant[106]. However, in combination with the PDOS and net spin moments previously discussed, we believe this small change to be further evidence for the $Ni^{2+} \rightarrow Ni^{4+}$ transition. Upon further charging, Ni atoms experience no additional change.

For O atoms, Fig. 9b illustrates several interesting points. First, as with Ni, we can see a change ($\sim$0.2e) occur for the desodiation process and no change for perchlorate intercalation. Although such a change has been previously reported as insignificant[106], combining this change with those observations in the PDOS corroborates a $O^{2-} \rightarrow O^{-}$ transition. As previously discussed for the PDOS in Sec. 3.4.1, Fig. 9b shows O atoms within ClO_4 exhibiting interesting behavior. For some of these atoms (which are denoted by the red circles), the calculated Bader charge seemingly demonstrates further redox activity. However, this is difficult to determine as the ClO_4 O's have no previous values to compare to; their Bader charges may simply be the result of computational artifacts and should not be taken as claim of redox activity.

As previously stated, utilizing a single method is not sufficient for investigating charge compensation redox reactions, as evident by the minimal change in Bader charge for Ni and O atoms. While PDOS, the DDEC6 method, and Bader charge analysis provide insight into the electronic nature of a material, sometimes a simple structural analysis can prove insightful as well. Therefore, the changes in various X–O (X = Mn, Ni, O) bonds were investigated for structural (octahedron) distortions as evidence of redox activity.

3.4.4 X–O Bond Changes

As structural distortions (*i.e.*, bond length changes) have been previously reported as evidence of redox activity[46,49,106,107,109,114,115], we include such a method to complement the electronic structure analyses from Sec. 3.4.1–3.4.3 and conclude our investigation of the charge compensation response of NMO. To accomplish this, the radial distribution function, $g(r)$, was individually determined for Mn–O, Ni–O, and O–O bonds with the Open Visualization Tool (OVITO)[116]. Each of these bond types are separately plotted for the fully sodiated, empty, and fully perchlorated systems.

The Mn–O and Ni–O bonds are shown in Fig. 10a & 10b, respectively. These two bond types are discussed most succinctly. The Mn–O bonds show no change throughout charging, indicative of no redox activity for these atoms. Conversely, the Ni–O bonds show a distinct shortening during desodiation and no change for perchlorate intercalation, indicating redox activity of these atoms during desodiation. These results further corroborate those previously discussed.

The O–O bond changes are shown in Fig. 11. While a great deal is shown, we will break down the changes based on our categorization of these bonds, which are all shown individually in Sec. S8†. As with the Mn–O and Ni–O bonds, O–O bonds show no change during charging from empty to fully perchlorated (*i.e.*, red and gray lines, respectively, in Fig. 11). Therefore, the following discussion refers exclusively to the desodiation process.

We first focus on the black arrow in Fig. 11, which points to the peaks ($\sim$2.5 & 2.7 Å) corresponding to O atoms diagonal from one another in the NiO_6 octahedra (Fig. S10a†). These bonds shorten from 2.7 to 2.5 Å during desodiation. Similarly, O atoms within the same plane of the NiO_6 octahedra (Fig. S10b†) experience a shortening from $\sim$3.05 to 2.8 Å (denoted by green arrows). As these two O–O bond types shorten within the NiO_6 octahedra, a bond type within the MnO_6 octahedra must lengthen to compensate. This is shown by the purple arrows, which correspond

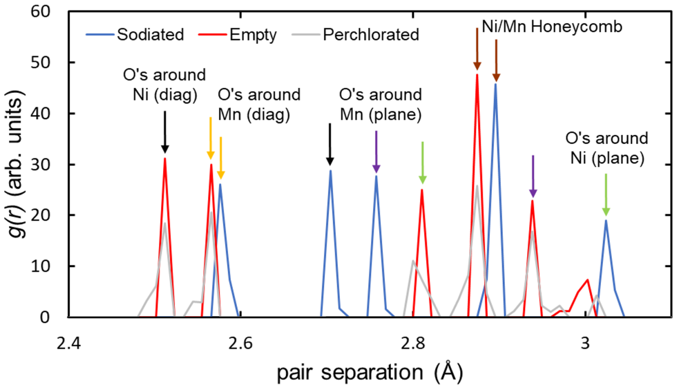

Fig. 11 Radial distribution plots of O–O bonds within the fully sodiated, empty, and fully perchlorated structures when relaxed with PBE-D3+U. Included are colored arrows denoting peaks corresponding to the same type of O atoms across the different systems (see Sec. S8† for figures of the classifications of O atoms).

to O atoms in the same plane around Mn (Fig. S10c†). Those investigated bond types which experienced no significant change are O atoms diagonally around Mn atoms (orange arrows) and those we coined as "honeycomb" (brown arrows); both of these are shown in Fig. S10d and Fig. S10e†, respectively.

Taking these data into consideration, it is evident the Mn–O bonds experience minimal change in length. Based on this, we would expect no redox activity for Mn or O (at least for those coordinated around Mn) throughout the charging process. For Ni–O bonds, a clear shortening occurs, indicating that one (or both) of the involved species undergo an electronic change during desodiation. Such a change from cation concentration alone has been shown in other investigations as well[46,49,106,107,109,114,115]. The results for the Mn–O and Ni–O bond types are further corroborated through the O–O bond length investigation. Here, O atoms coordinated around Ni experience a shortening of their bonds in two different directions, providing further evidence that a concurrent redox mechanism occurs for both species. Additionally, the O atoms coordinated around Mn only experience a change in bond length as to compensate for those structural changes occurring within the neighboring NiO_6 octahedra.

Due to only investigating the sodiated and perchlorated structures (*i.e.*, the starting and ending point for the full charging process), it is of no surprise that Li *et al.*[25] found evidence of Ni and O redox. However, as with the charging mechanism, we propose it is in actuality a simultaneous occurrence. As such, one may ask what then compensates for the addition of charge during perchlorate intercalation. An intriguing observation within our DOS and Bader charge calculations was that the O atoms within ClO_4 appear to become oxidized upon intercalation. However, the definitive claim of ClO_4 redox activity cannot be made without further analysis, which remains to be carried out in future work. This is where we further believe a simultaneous charging mechanism occurs, leading to no independent charge compensation required for anion intercalation as such a process does not occur on its own; Ni and O atoms undergo redox throughout the charging mechanism solely due to cation involvement.

4 Conclusion

Through our computational investigation of Na deintercalation and ClO_4 intercalation within the $Ni_{0.25}Mn_{0.75}O_2$ cathode material, several key insights were uncovered. First, we proposed a novel method for computationally determining the voltage associated with anion intercalation. While other methods exist for determining the voltage from anion intercalation, ours is the first to fully account for all solvent/salt interactions within the electrolyte. Through this novel method, voltages were calculated for a variety of pathways to charge from $Na_{0.5}Ni_{0.25}Mn_{0.75}O_2$ to $Ni_{0.25}Mn_{0.75}O_2(ClO_4)_{0.167}$. It was determined that a novel simultaneous cation (Na) deintercalation and anion (ClO_4) intercalation charging mechanism occurs within this material, providing an alternative interpretation to previous reports. A major contribution to this charging mechanism of $Ni_{0.25}Mn_{0.75}O_2$ is the charge compensation redox reactions of $Ni^{2+} \rightarrow Ni^{4+}$ and $O^{2-} \rightarrow O^{-}$. Evidence of both oxidation state transitions was found through plotting of density of states, determination of net atomic spin moments, Bader charge analyses, and changes to X–O (X = Mn, Ni, O) bond lengths leading to structural distortions. However, our calculations show that these reactions occur simultaneously as a result of cation deintercalation and not due to anion intercalation.

In order to meet the ever-growing demand for batteries, it is essential to develop a toolkit from which we can select the next-generation batteries. In recent years, we have seen great advancements in building our battery toolkit with solid-state batteries, multivalent ion batteries, Li-air batteries, sulfur batteries, and beyond. In this study, we show that simultaneous dual-ion charging is a characteristic that can enhance battery performance and should be included in our growing repository of next-generation batteries.

Conflicts of interest

There are no conflicts to declare.

Acknowledgements

This work was supported by the National Science Foundation under grant number CBET-2028722. The calculations were performed using the *Expanse* computing cluster, a part of the Extreme Science and Engineering Discovery Environment (XSEDE, supported by National Science Foundation grant number ACI-1548562) under the allocation TG-DMR180009, as well as the *Spiedie* high-performance computing cluster at Binghamton University.

Notes and references

1 USP4668595, (1985); A. Yoshino, K. Sanechika, T. Nakajima, JP1989293, (1985).

2 M. S. Whittingham, Science, 1976, **192**, 1126–1127.

3 H. Ikeda, T. Saito and H. Tamaru, Denki Kagaki, 1977, **45**, 314–318.

4 H. Ikeda, T. Saito and H. Tamaru, Denki Kagaku, 1977, **45**, 391–395.

5 EP17400B1, (1979); Goodenough, J. B. and Mizushima, K. and Wiseman, P. J.

6 K. Mizushima, P. Jones, P. Wiseman and J. Goodenough, Mater. Res. Bull., 1980, **15**, 783–789.

7 R. Yazami and P. Tauzain, J. Power Sources, 1983, **9**, 365–371.

8 R. Van Noorden, Nature, 2014, **507**, 26–28.

9 M. S. Whittingham, Chem. Rev., 2004, **104**, 4271–4301.

10 M. S. Whittingham, MRS Bull., 2008, **33**, 411–419.

11 T. R. Juran and M. Smeu, Phys. Chem. Chem. Phys., 2017, **19**, 20684–20690.

12 T. R. Juran, J. Young and M. Smeu, J. Phys. Chem. C, 2018, **122**, 8788–7895.

13 J. Young and M. Smeu, J. Phys. Chem. Lett., 2018, **9**, 3295–3300.

14 J. Young, P. M. Kulick, T. R. Juran and M. Smeu, ACS Appl. Energy Mater., 2019, **2**, 1676–1684.

15 T. R. Juran and M. Smeu, J. Power Sources, 2019, **436**, 226813.

16 R. Shepard and M. Smeu, J. Power Sources, 2020, **472**, 228096.

17 D. R. Lide, CRC Handbook of Chemistry and Physics, CRC Press, Boca Raton, Florida, 85th edn, 2005.

18 E. A. Olivetti, G. Cedar, G. G. Gaustad and X. Fu, Joule, 2017, **1**, 229–243.

19 N. A. Chernova, M. Roppolo, A. C. Dillon and M. S. Whittingham, J. Mater. Chem., 2009, **19**, 2526–2552.

20 S. P. Ong, V. L. Chevrier, G. Hautier, A. Jain, C. Moore, S. Kim, X. Ma and G. Ceder, Energy Environ. Sci., 2011, **4**, 3680–3688.

21 M. S. Islam and C. A. J. Fisher, Chem. Soc. Rev., 2014, **43**, 185–204.

22 P. Canepa, G. S. Gautam, D. C. Hannah, R. Malik, M. Liu, K. G. Gallagher, K. A. Persson and G. Ceder, Chem. Rev., 2017, **117**, 4287–4341.

23 J. Ding, Y.-C. Lin, J. Liu, J. Rana, H. Zhang, H. Zhou, I.-H. Chu, K. M. Wiaderek, F. Omenya, N. A. Chernova, K. W. Chapman, L. F. J. Piper, S. P. Ong and M. S. Whittingham, Adv. Energy Mater., 2018, **8**, 1800221.

24 J.-Y. Hwang, S.-T. Myung and Y.-K. Sun, Chem. Soc. Rev., 2017, **46**, 3529–3614.

25 Q. Li, Y. Qiao, S. Guo, K. Jiang, Q. Li, J. Wu and H. Zhou, Joule, 2018, **2**, 1134–1145.

26 K. Tasaki, J. Phys. Chem. C, 2014, **118**, 1443–1450.

27 E. Zhang, W. Cao, B. Wang, X. Yu, L. Wang, Z. Xu and B. Lu, Energy Storage Mater., 2018, **11**, 91–99.

28 L. Xing, O. Borodin, G. D. Smith and W. Li, J. Phys. Chem. A, 2011, **115**, 13896–13905.

29 Y. Terashima, K. Takeda and M. Honda, Chem. Phys., 2014, **430**, 23–28.

30 M. El Kazzi, I. Czekaj, E. J. Berg, P. Novák and M. A. Brown, Top. Catal., 2016, **59**, 628–634.

31 S. Kheirjou and A. Fattahi, J. Phys. Org. Chem., 2017, **31**, e3798.

32 P. Hohenberg and W. Kohn, Phys. Rev., 1964, **136**, B864–B871.

33 W. Kohn and L. J. Sham, Phys. Rev., 1965, **140**, A1133–A1138.

34 J. P. Perdew and A. Zunger, Phys. Rev. B, 1981, **23**, 5048–5079.

35 S. Lundqvist and N. H. March, Theory of the Inhomogeneous Electron Gas, Plenum, New York, 1st edn, 1983.

36 W. Kohn, A. D. Becke and R. G. Parr, J. Phys. Chem., 1996, **100**, 12974–12980.

37 W. Koch and M. C. Holthausen, A Chemist's Guide to Density Functional Theory, Wiley-VCH, Weinheim, 2nd edn, 2001.

38 K. Capelle, Braz. J. Phys., 2006, **36**, 1318–1348.

39 J. P. Perdew, K. Burke and M. Ernzerhof, Phys. Rev. Lett., 1996, **77**, 3865–3868.

40 J. Sun, A. Ruzsinszky and J. P. Perdew, Phys. Rev. Lett., 2015, **115**, 036402.

41 S. Grimme, J. Antony, S. Ehrlich and H. Krieg, J. Chem. Phys., 2010, **132**, 154104.

42 R. Sabatini, T. Gorni and S. De Gironcoli, Phys. Rev. B, 2013, **87**, 041108(R).

43 H. Peng, Z.-H. Yang, J. Sun and J. P. Perdew, Phys. Rev. X, 2016, **6**, 041005.

44 V. I. Anisimov, J. Zaanen and O. K. Andersen, Phys. Rev. B, 1991, **44**, 943–954.

45 S. L. Dudarev, G. A. Botton, S. Y. Savrasov, C. J. Humphreys and A. P. Sutton, Phys. Rev. B, 1998, **57**, 1505–1509.

46 M. Saubanère, E. McCalla, J.-M. Tarascon and M.-L. Doublet, Energy Environ. Sci., 2016, **9**, 984–991.

47 P. E. Pearce, A. J. Perez, G. Rousse and M. Saubanere, Nature Mater., 2017, **16**, 580–586.

48 J. Zheng, G. Teng, J. Yang, M. Xu, Q. Yao, Z. Zhuo, W. Yang, Q. Liu and F. Pan, J. Phys. Chem. Lett., 2018, **9**, 6262–6268.

49 D. Kim and J. Lee, Chem. Mater., 2020, **32**, 5541–5549.

50 W. Zuo, F. Ren, Q. Li and X. Wu, Nano Energy, 2020, **78**, 105285.

51 G. Kresse and J. Furthmüller, Phys. Rev. B, 1996, **54**, 11169–11186.

52 P. E. Blöchl, Phys. Rev. B, 1994, **50**, 17953–17979.

53 H. J. Monkhorst and J. D. Pack, Phys. Rev. B, 1976, **13**, 5188–5192.

54 M. Methfessel and A. T. Paxton, Phys. Rev. B, 1989, **40**, 3616–3621.

55 P. E. Blöchl, O. Jepsen and O. K. Andersen, Phys. Rev. B, 1994, **49**, 16223–16233.

56 W. H. Press, S. A. Teukolsky, W. T. Vetterling and B. P. Flannery, Numerical Recipes: The Art of Scientific Computing, Cambridge University Press, New York, 3rd edn, 2007.

57 K. Momma and F. Izumi, J. Appl. Crystallogr., 2011, **44**, 1272–1276.

58 G. Mills and H. Jónsson, Phys. Rev. Lett., 1994, **72**, 1124–1127.

59 G. Mills, H. Jónsson and G. K. Schenter, Surf. Sci., 1995, **324**, 305–337.

60 G. Henkelman and H. Jónsson, J. Chem. Phys., 2000, **113**, 9978–9985.

61 G. Henkelman and H. Jónsson, Phys. Rev. Lett., 2001, **86**, 664–667.

62 G. Henkelman, G. Jóhannsesson and H. Jónsson, Schwartz S. D. (eds) Theoretical Methods in Condensed Phase Chemistry. Progress in Theoretical Chemistry and Physics, Springer, Dordrecht, 2002, vol. 5, pp. 269–302.

63 D. Sheppard, R. Terrell and G. Henkelman, J. Chem. Phys., 2008, **128**, 134106.

64 D. Sheppard and G. Henkelman, J. Comput. Chem., 2011, **32**, 1769–1771.

65 D. Sheppard, P. Xiao, W. Chemelewski, D. D. Johnson and G. Henkelman, J. Chem. Phys., 2012, **136**, 074103.

66 R. Car and M. Parrinello, Phys. Rev. Lett., 1985, **55**, 2471–2474.

67 R. Car and M. Parrinello, Phy. Rev. Lett., 1988, **60**, 204–207.

68 K. Laasonen, R. Car, C. Lee and D. Vanderbilt, Phys. Rev. B, 1991, **43**, 6796–6799.

69 G. Pastore, E. Smargiassi and F. Buda, Phys. Rev. A, 1991, **44**, 6334–6347.

70 *Propylene Carbonate*; MSDS No. 310328 [Online]; Sigma-Aldrich Inc.: St. Louis, MO, Nov 20, 2020.

71 K. Kuratani, N. Uemura, H. Senoh, H. T. Takeshita and T. Kiyobayashi, J. Power Sources, 2013, **223**, 175–182.

72 S. Nosé, J. Chem. Phys., 1984, **81**, 511–519.

73 W. G. Hoover, Phys. Rev. A, 1985, **31**, 1695–1697.

74 S. Nosé, Prog. Theor. Phys. Suppl., 1991, **103**, 1–46.

75 D. Frenkel and B. Smit, Understanding Molecular Smulation: From Algorithms to Applications, Academic Press, London, 1996.

76 D. Frenkel and B. Smit, Understanding Molecular Simulation: From Algorithms to Applications, Academic Press, San Diego, 2nd ed., 2002.

77 R. K. Pathria and P. D. Beale, Statistical Mechanics, Elsevier, Boston, 3rd ed., 2011.

78 M. K. Aydinol, A. F. Kohan, G. Ceder, K. Cho and J. Joannopoulos, Phy. Rev. B, 1997, **56**, 1354–1365.

79 M. K. Aydinol, A. F. Kohan and G. Ceder, J. Power Sources, 1997, **68**, 664–668.

80 M. K. Aydinol and G. Ceder, J. Electrochem. Soc., 1997, **144**, 3832–3835.

81 E. Deiss, A. Wokaun, J.-L. Barras, C. Daul and P. Dufek, J. Electrochem. Soc., 1997, **144**, 3877–3881.

82 S. K. Mishra and G. Ceder, Phys. Rev. B, 1999, **59**, 6120–6130.

83 G. Ceder and A. Van Der Ven, Electrochim. Acta, 1999, **45**, 131–150.

84 Y. S. Meng and M. E. Arroyo-De Dompablo, Energy Environ. Sci., 2009, **2**, 589–609.

85 P. Bhauriyal, A. Mahata and B. Pathak, Phys. Chem. Chem. Phys., 2017, **19**, 7980–7989.

86 K. V. Kravchyk, P. Bhauriyal, L. Piveteau, C. P. Guntlin, B. Pathak and M. V. Kovalenko, Nat. Commun., 2018, **9**, 4469.

87 S. Kumar, P. Bhauriyal and B. Pathak, J. Phys. Chem. C, 2019, **123**, 23863–23871.

88 X. Xiao, M. Wang, J. Tu and S. Jiao, Phys. Chem. Chem. Phys., 2019, **21**, 7021–7028.

89 H. Saini, S. Das and B. Pathak, Mater. Adv., 2020, **1**, 2418–2425.

90 M. L. Agiorgousis, Y.-Y. Sun and S. Zhang, ACS Energy Lett., 2017, **2**, 689–693.

91 T. A. Manz and D. S. Sholl, J. Chem. Theory Comput., 2010, **6**, 2455–2468.

92 T. A. Manz and D. S. Sholl, J. Chem. Theory Comput., 2011, **7**, 4146–4164.

93 T. A. Manz and D. S. Sholl, J. Chem. Theory Comput., 2012, **8**, 2844–2867.

94 T. A. Manz and N. G. Limas, arXiv, 2015, 1–97.

95 T. A. Manz and N. G. Limas, RSC Adv., 2016, **6**, 47771–47801.

96 N. G. Limas and T. A. Manz, RSC Adv., 2016, **6**, 45727–45747.

97 T. A. Manz, RSC Adv., 2017, **7**, 45552–45581.

98 N. G. Limas and T. A. Manz, RSC Adv., 2018, **8**, 2678–2707.

99 T. A. Manz, T. Chen, D. J. Cole, N. G. Limas and B. Fiszbein, ChemRxiv, 2018, 1–57.

100 U. Müller, Inorganic Structural Chemistry, John Wiley & Sons Inc., New Jersey, 2nd edn, 2006.

101 Z. Rong, R. Malik, P. Canepa, G. Sai Gautam, M. Liu, A. Jain, K. Persson and G. Ceder, Chem. Mater., 2015, **27**, 6016–6021.

102 M. Woodcox, R. Shepard and M. Smeu, J. Power Sources, 2021, **516**, 230620.

103 D. Liepinya, R. Shepard and M. Smeu, Comp. Mater. Sci., 2022, **202**, 110948.

104 X. Qi, B. Blizanac, A. DuPasquier, P. Meister, T. Placke, M. Oljaca, J. Li and M. Winter, Phys. Chem. Chem. Phys., 2014, **16**, 25306–25313.

105 M. Wang and Y. Tang, Adv. Energy Mater., 2018, **8**, 1703320.

106 A. Massaro, A. B. M. noz García, P. P. Prosini, C. Gerbaldi and M. Pavone, ACS Energy Lett., 2021, **6**, 2470–2480.

107 M. Kim, H. Kim, M. Cho and D. Kim, J. Mater. Chem. A, 2021, **9**, 15179–15187.

108 M. D. Johannes, K. Swider-Lyons and C. T. Love, Solid State Ion., 2016, **286**, 83–89.

109 J.-H. Park, I.-H. Ko, J. Lee and S. Park, ChemElectroChem, 2021, **8**, 625–643.

110 G. Choi, J. Lee and D. Kim, ACS Appl. Mater. Interfaces, 2020, **12**, 29203–29211.

111 H. Yu, Y. Qian, M. Otani and D. Tang, Energy Environ. Sci., 2014, **7**, 1068–1078.

112 F. A. Cotton and G. Wilkinson, Adavnced Inorganic Chemistry: A Comprehensive Text, Wiley InterScience, New York, 4th edn, 1980.

113 T. Saito, Inorganic Chemistry, CreateSpace Independent Publishing Platform, South Carolina, 2014.

114 M. B. Yahia, J. Vergnet, M. Saubanère and M.-L. Doublet, Nature Mater., 2019, **18**, 496–502.

115 J. Vergnet, M. Saubanère, M.-L. Doublet and J.-M. Tarascon, Joule, 2020, **4**, 420–434.

116 A. Stukowski, Modelling Simul. Mater. Sci. Eng., 2010, **18**, 015012.